

Likelihood-Separable Diffusion Inference for Multi-Image MRI Super-Resolution

Samuel W. Remedios
Johns Hopkins University
Baltimore, MD, USA
samuel.remedios@jhu.edu

Aaron Carass
Johns Hopkins University
Baltimore, MD, USA

Zhangxing Bian
Johns Hopkins University
Baltimore, MD, USA

Jerry L. Prince
Johns Hopkins University
Baltimore, MD, USA

Shuwen Wei
Johns Hopkins University
Baltimore, MD, USA

Blake E. Dewey
Johns Hopkins University
Baltimore, MD, USA

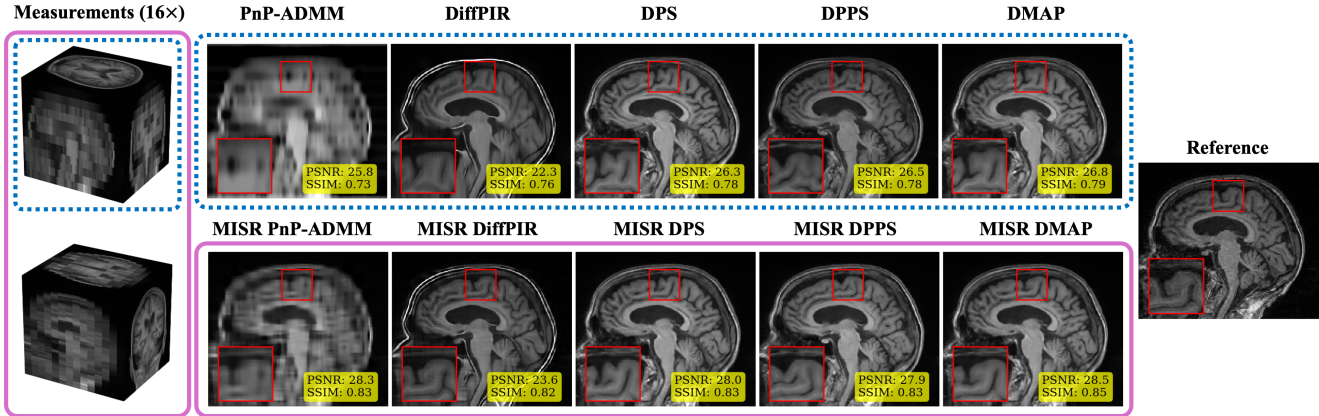


Figure 1. **Overview of our proposed MISR generalization to diffusion super-resolution.** Our method generalizes existing methods for multi-image super-resolution (MISR). The first column shows low-resolution (LR) anisotropic MRI measurements with $16\times$ downsampling along orthogonal planes. For super-resolution results, the first row shows the existing methods for single-image super-resolution (SISR), which only use the LR measurement enclosed in the blue dotted box. The second row shows results for our proposed generalization of each method for MISR, which use both LR measurements enclosed in the pink solid box. All methods used the same 3D volumetric diffusion model, and all results are 3D volumetric images. A single sagittal slice is shown for viewing clarity. Volumetric PSNR and SSIM are overlaid in the yellow box, and zoomed inset regions are shown in red. MISR improves performance for all methods and better estimates the anatomy of the reference image, shown on the far right.

Abstract

Diffusion models are the current state-of-the-art for solving inverse problems in imaging. Their impressive generative capability allows them to approximate sampling from a prior distribution, which alongside a known likelihood function permits posterior sampling without retraining the model. While recent methods have made strides in advancing the accuracy of posterior sampling, the majority focuses on single-image inverse problems. However, for modalities such as magnetic resonance imaging (MRI), it is common to acquire multiple complementary measurements, each low-resolution

along a different axis. In this work, we generalize common diffusion-based inverse single-image problem solvers for multi-image super-resolution (MISR) MRI. We show that the DPS likelihood correction allows an exactly-separable gradient decomposition across independently acquired measurements, enabling MISR without constructing a joint operator, modifying the diffusion model, or increasing network function evaluations. We derive MISR versions of DPS, DMAP, DPPS, and diffusion-based PnP/ADMM, and demonstrate substantial gains over SISR across $4\times/8\times/16\times$ anisotropic degradations. Our results achieve state-of-the-art super-resolution of anisotropic MRI volumes and, critically, en-

able reconstruction of near-isotropic anatomy from routine 2D multi-slice acquisitions, which are otherwise highly degraded in orthogonal views.

1. Introduction

Super-resolution (SR) is a linear inverse problem that estimates a candidate high-resolution (HR) image given an observed low-resolution (LR) image [2, 5, 9, 11, 17, 18, 20, 23–25, 27, 31, 35, 37, 41–43, 47, 48, 59, 61–67, 69–71]. Mathematically, SR uses the observed LR image $y \in \mathbb{R}^m$ (the *measurement*) to estimate the HR image $x \in \mathbb{R}^n$ given the forward model

$$y = Ax + \epsilon, \quad (1)$$

where $A \in \mathbb{R}^{m \times n}$ is the linear forward operator and $\epsilon \sim \mathcal{N}(0, \sigma \mathbf{I}_m)$. Since $m < n$, Eq. 1 is underdetermined and noisy, multiple solutions exist; the problem is *ill-posed*. Some form of regularization is required to select a solution.

While classical approaches use hand-crafted regularization priors such as total variation [61, 70] or sparsity under some transform [6, 21, 49, 51], contemporary data-driven approaches use denoisers as a plug-and-play prior [12, 32, 33, 55, 60]. This practice began with generic denoising algorithms [8, 46, 58] but has recently found deep theoretic connections with the family of diffusion models, including denoising diffusion probabilistic models (DDPMs) [29], score-based models [56], flow models [26, 40], and Schrödinger bridges [19, 52]. These approaches learn a generative model that transforms samples from one distribution (often a high-dimensional standard Gaussian) to the data distribution. In this way, diffusion models act as a Bayesian prior on the desired data distribution $p(x)$. Accordingly, inverse problem solving algorithms leverage Bayes' rule to sample from the posterior:

$$p(x|y) \propto p(y|x)p(x), \quad (2)$$

where the likelihood term $p(y|x)$ is approximated by the known measurement function Eq. 1.

This insight has spurred great developments in the use of diffusion models for inverse problem solving. The recipe for solving any inverse problem with Eq. 2 requires only three ingredients: a known forward operator A , a pretrained diffusion model to approximate $p(x)$, and a technique to sample from the posterior $p(y|x)p(x)$. Most works assume that A is known, assume the distribution of ϵ is known, and use an existing well-trained diffusion model. Thus, algorithm development focuses on the sampling procedure. Diffusion Posterior Sampling (DPS) [15], which corrects samples on the diffusion trajectory towards the data-consistent manifold via a gradient update, is possibly the most well-known.

Most work on SR has focused on single-measurement inverse problem solving. However, in problem settings such as

magnetic resonance imaging (MRI), multiple measurements are common. For example, an MRI session may include multiple scans along orthogonal axes. These occur for a multitude of reasons, such as improving signal-to-noise ratio, mitigating motion artifacts, or due to special MRI pulse sequences designed for slice-wise acquisition. Such sessions often result in multiple image volumes that are HR along two axes (called *in-plane*) but LR along the third axis (the *through-plane*). These *anisotropic* image volumes are faster to acquire, but by trading signal-to-noise (SNR) and in-plane resolution for a degraded through-plane resolution, the image volumes are not clinically useful when viewed through-plane. Radiologists therefore do not read anisotropic volumes in the through-planes, as important anatomical structures are blurred and/or decimated.

To leverage the complementary information available in this real-world setting, we propose to generalize diffusion inverse problem solving approaches for the multi-image super-resolution (MISR) problem. In this paper, we show that diffusion models can accurately estimate the underlying isotropic anatomy without retraining for specific resolutions. To our knowledge, no prior work in MRI or diffusion inverse problems has shown that multiple anisotropic volumes can be restored to isotropy. This positions MISR diffusion as a practical, high-impact alternative to long 3D MRI scans.

Our main contributions are as follows:

- **Likelihood separability for diffusion posterior sampling.** We show that the likelihood gradient decomposes exactly across independent measurements, permitting MISR correction using only per-measurement operators. This enables multi-image posterior correction without a joint operator or modification of the diffusion model.
- **A unified MISR generalization of diffusion inverse solvers.** We derive MISR versions of DPS, DMAP, DPPS, and diffusion-based PnP/ADMM.
- **Noise weighting for heterogeneous MRI acquisitions.** We introduce inverse-variance weighting of per-measurement gradients, enabling principled fusion of measurements with different slice thicknesses, SNRs, and spatial resolutions.
- **State-of-the-art MISR MRI performance.** Across $4 \times / 8 \times / 16 \times$ through-plane degradations, our MISR extensions substantially outperform their single-image counterparts, improving PSNR by 1 to 3 dB while producing anatomically faithful reconstructions. Evaluations were conducted with 64 network function evaluations (NFEs) for the reverse diffusion process, yielding a total super-resolution time per volume of less than 60 seconds on an NVIDIA RTX 6000 ADA.

When taken together, our contributions establish diffusion models as a practical, flexible, and high-quality approach for multi-image MRI super-resolution without retraining.

2. Background

2.1. Diffusion models

Diffusion-based models are the current state of the art in generative modeling [7]. They include the denoising diffusion probabilistic model (DDPM) [29], the denoising diffusion implicit model (DDIM) [54], score-based models [14, 15], Schrödinger bridges [10, 52, 57], and Brownian bridges [13, 34, 36]. There are also connections between diffusion-based models and flow matching [26, 38, 39].

Diffusion models establish a Markov chain of transition states between the data distribution and a noise distribution, typically a high-dimensional Gaussian. By convention, we will denote a state at the data distribution by x_0 and a state at the noise distribution by x_1 . Thus, arbitrary transition states are denoted by x_t for $t \in [0, 1]$. A state x_s is closer to the data distribution than x_t whenever $s < t$. The forward diffusion process describes how data diffuses into noise and is of closed form. The reverse diffusion process describes how to denoise each transition state and is parameterized by a neural network. The goal in training a diffusion model is to find parameters θ that allow the neural network $f_\theta(x_t, t)$ to move from transition state x_t at time t to a less-noisy state x_s . Once trained, at inference time, a sample x_1 is drawn and successively transformed through a series of transition states until arriving at the data state x_0 .

The forward diffusion process defines x_t as a linear combination between data and noise:

$$x_t = \alpha_t x_0 + \beta_t \epsilon, \quad (3)$$

where α_t and β_t are parameters for the noise schedule and $\epsilon \sim \mathcal{N}(\mathbf{0}, \mathbf{I})$ by definition. The reverse diffusion process is the following:

$$x_s = \alpha_s \hat{x}_0 + \beta_s \hat{\epsilon}, \quad (4)$$

where $\hat{\epsilon} = (x_t - \alpha_t \hat{x}_0) / \beta_t$ and \hat{x}_0 is estimated by the diffusion network f_θ . Equation 4 is the DDIM sampler [53], which generalizes the DDPM framework [29] and allows accelerated and deterministic sampling. The full reverse diffusion process arrives at $t = 0$ by iteratively applying Eq. 4.

While the methods presented in this paper are agnostic to the specific way \hat{x}_0 is obtained (sample estimation, noise estimation, velocity estimation, etc. [26]), our work will specifically make use of the flow estimation framework [26, 38, 39]. That is, the network f_θ estimates the flow-matching field: $\hat{u} = \hat{\epsilon} - \hat{x}_0 = f_\theta(x_t, t)$, so

$$\hat{x}_0 = \hat{\epsilon} - f_\theta(x_t, t) \quad (5)$$

and

$$\hat{\epsilon} = f_\theta(x_t, t) + \hat{x}_0. \quad (6)$$

Due to the empirical success of diffusion models, much theoretical work has been done to connect schools of thought.

There are now many leading perspectives on diffusion models, including the score, variational, flow-matching, and Schrödinger bridge perspectives.

2.2. 2D Magnetic Resonance Image Acquisition

In MRI, image volumes are rarely obtained alone. Usually, imaging sessions acquire multiple images of different contrasts, orientations, and resolutions. We will consider the common scenario of an MRI session where the same pulse sequence is used to acquire multiple images along orthogonal axes, each potentially with different slice thicknesses. In this case, image volumes are formed by *2D acquisition* (also called *2D MRI* or *2D multi-slice MRI*). In 2D MRI acquisitions, samples are acquired in 2D k-space after exciting a slab within the field of view using slice selection [4]. Different regions are selected by varying the slice selection parameters, resulting in a set of independently acquired slices. Each of these slices is converted to the image domain with the inverse Fourier transform and then stacked along the through-plane axis to create a 3D volume.

Slice selection determines the through-plane resolution. The physics of slice selection allow us to write the relationship between HR and LR images along one dimension. In Eq. 1, A can be written as a strided convolution using the slice selection profile and the separation between slices in millimeters. In practice, the slice selection profile is proprietary and its closed-form equation is unknown. However, it is known that a Gaussian kernel serves as a reliable approximation. In this work, we assume that the slice selection uses Gaussian profiles with slice separations and full-width-at-half-maxes equal to the scale factor.

2.3. Diffusion posterior sampling for SISR

Diffusion Posterior Sampling (DPS)[15] uses Jensen's approximation for the likelihood term in Eq. 2: $p(y | x_t) \approx p(y | \mathbb{E}[x_0 | x_t])$. This is convenient, since computing $\mathbb{E}[x_0 | x_t]$ is a conventional step in the reverse diffusion process (see Eq. 5). With this, DPS adjusts samples x_s in the diffusion process towards the data-consistent manifold:

$$x_s - \nabla_{x_t} \| A \mathbb{E}[x_0 | x_t] - y \| \quad (7)$$

The algorithm for implementing DPS is shown in Algorithm 1. It should be noted that DPS does not require the forward operator to be linear, only differentiable.

Many methods have built on this initial formulation from DPS. We defer the reader to [16] for further reading, but briefly summarize a few methods here. The denoising diffusion null-space model (DDNM) does a state-wise correction with a hard projection for linear forward operators. Diffusion plug-and-play image restoration (DiffPIR) uses the proximal algorithm half-quadratic splitting to update diffusion states to be proximal to the observation. Diffusion posterior proximal sampling (DPPS) samples multiple candidates at

each state x_t and selects the one with the smallest distance to the data-consistent manifold. Diffusion Maximum A Posteriori (DMAP) performs multiple sampling steps to better approximate a MAP sample.

3. Method

Our objective is to generalize diffusion priors to the multi-image super-resolution (MISR) problem. We first formalize the MISR observation model and derive a separable likelihood expression that permits multi-image data consistency without constructing a joint operator. We then analyze the implications of this decomposition for DPS and describe MISR extensions of several existing solvers, including DPS, DMAP, DPPS, and diffusion-based PnP methods.

3.1. MISR Preliminaries

We seek a single HR image $x \in \mathbb{R}^n$ that is consistent with multiple LR measurements $\{y_i \in \mathbb{R}^{m_i}\}_{i=1}^N$. This yields a set of equations:

$$y_i = A_i x + \epsilon_i, \quad (8)$$

where $A_i \in \mathbb{R}^{m_i \times n}$ and $\epsilon_i \sim \mathcal{N}(0, \sigma_i \mathbf{I}_{m_i})$. Since all operations are linear, it is possible to rewrite Eq. 8 as

$$\underline{y} = \underline{A}x + \underline{\epsilon}, \quad (9)$$

where $\underline{y} = [y_1 \ \dots \ y_N]^\top$, $\underline{A} = [A_1 \ \dots \ A_N]^\top$, and $\underline{\epsilon} = [\epsilon_1 \ \dots \ \epsilon_N]^\top$. Although \underline{A} is mathematically well-defined, in MRI each A_i may operate on different grids with different slice geometries, making explicit stacking computationally impractical.

3.2. Likelihood separability in DPS

The joint negative log-likelihood of Eq. 8 is

$$\mathcal{L}(x) = \sum_{i=1}^N \frac{1}{2\sigma_i^2} \|A_i x - y_i\|_2^2, \quad (10)$$

which is separable across observations.

Proposition 1. *Let $\mu_0(x_t) = \mathbb{E}[x_0 \mid x_t]$ be the diffusion model's estimation of the data sample from time t . Then, the likelihood gradient to correct x_t towards the data consistent manifold is*

$$\nabla_{x_t} \mathcal{L}(\mu_0(x_t)) = \sum_{i=1}^N \frac{1}{\sigma_i^2} \nabla_{x_t} \|A_i \mu_0(x_t) - y_i\|_2^2. \quad (11)$$

In particular, each A_i contributes an independent correction direction, and the combined gradient is their sum.

Proof. By independence of measurements,

$$\mathcal{L}(\mu_0) = \sum_{i=1}^N \mathcal{L}_i(\mu_0). \quad (12)$$

Since the diffusion network f_θ is used only to generate $\mu_0(x_t)$ and the measurement operators A_i are linear and do not couple measurements,

$$\nabla_{x_t} \mathcal{L}(\mu_0(x_t)) = \sum_{i=1}^N \nabla_{x_t} \mathcal{L}_i(\mu_0(x_t)). \quad (13)$$

With substitution,

$$\nabla_{x_t} \mathcal{L}(\mu_0(x_t)) = \sum_{i=1}^N \frac{1}{\sigma_i^2} \nabla_{x_t} \|A_i \mu_0(x_t) - y_i\|_2^2 \quad (14)$$

□

Remark. Proposition 1 guarantees that MISR diffusion posterior sampling requires only independent per-measurement gradients without requiring a joint operator, modification of the diffusion model, nor an increase in NFEs. The nonlinearity of μ_0 does not break linear separability because dependence on μ_0 flows through the chain rule.

The separability of likelihoods under DPS has several implications. First, as we will demonstrate in this work, we can extend several approaches in the DPS family for MISR. Second, likelihood separability can generalize to any components that are independent in A , not just multiple observations. For example, in the SISR framework, we could split A into independent rows and consider different regions of images as separate measurements. This extends to further norm-preserving linear maps, and so block-stacked wavelet transform matrices could allow splitting by wavelet subband. We leave this exploration for future work. Finally, likelihood separability allows for independent weights for each component. With even weights, all measurements are considered equally. However, some measurements may be less reliable, for example, with more noise than others.

Algorithm 1 DPS

Require: T, A, y, ζ_t
1: $x_1 = \mathcal{N}(0, I)$
2: **for** $t = 1$ to 0 with T steps **do**
3: $x_s \sim p_\theta(X_s \mid x_t)$
4: $\mu_0 := \mathbb{E}[X_0 \mid x_t]$
5: $x_s = x_s - \zeta_t \nabla_{x_t} \|A \mu_0 - y\|$
6: **end for**
7: **return** x_0

Measurement noise weighting Each measurement may have its own noise strength; i.e., $\sigma_i \neq \sigma_j$ for $i \neq j$. In such scenarios, it is disadvantageous to correct states towards all observations equally. Thus, we propose to inversely scale the gradients by the strength of the noise for that observation.

Algorithm 2 MISR DPS

Require: $T, \{A_i\}_{i=1}^N, \{y_i\}_{i=1}^N, \{\sigma_i\}_{i=1}^N, \zeta_t$

- 1: $x_1 = \mathcal{N}(0, I)$
- 2: $w_i := (\sigma_i^2 + \sigma_{\text{floor}})^{-1}$
- 3: $w_i := N \cdot w_i / (\sum_{j=1}^N w_j)$
- 4: **for** $t = 1$ to 0 with T steps **do**
- 5: $x_s \sim p_\theta(X_s | x_t)$
- 6: $\mu_0 := \mathbb{E}[X_0 | x_t]$
- 7: $x_s = x_s - \zeta_t \nabla_{x_t} \sum_{i=1}^N [w_i \cdot \|A_i \mu_0 - y_i\|_2^2]$
- 8: **end for**
- 9: **return** x_0

3.3. MISR inverse diffusion methods

The previous sections provided a framework for MISR that is applicable to existing approaches. Here, we outline how these methods can be modified for noise-weighted MISR.

MISR DPS We describe MISR DPS in Algorithm 2. The gradient update term is weighted by $w_i: \nabla_{x_t} \sum_{i=1}^N [w_i \cdot \|A_i x_0|t - y_i\|_2^2]$, where $w_i \propto (\sigma_i^2 + \sigma_{\text{floor}})^{-1}$ and σ_{floor} is a noise floor that the diffusion model f_θ is robust to.

MISR DMAP DMAP uses multiple samples and gradient steps to refine the approximation of state s from state t . Since it is algorithmically similar to DPS (compare DPS in Algorithm 1 to DMAP in Algorithm 3), we are also able to generalize DMAP for MISR, shown in Algorithm 4.

MISR DPPS To implement MISR for DPPS, the selected candidate must have the smallest distance to all data-consistent manifolds.

MISR PnP Plug-and-play (PnP) methods that rely on priors are also amenable to MISR. The alternating direction method of multipliers (ADMM) uses variable splitting to optimize for data-consistency and prior-consistency [3]. The data-consistency term is still written as the squared ℓ_2 norm, so Eq. 11 is still applicable. The same logic applies to DiffPIR, with half-quadratic splitting instead of ADMM.

Algorithm 3 DMAP

Require: T, K, A, y, ζ_t, d

- 1: $x_1 = \mathcal{N}(0, I)$
- 2: **for** $t = 1$ to 0 with T steps **do**
- 3: $x_s \sim p_\theta(X_s | x_t)$
- 4: $\mu_s = \mathbb{E}[X_s | x_t]$
- 5: **for** $j = 1$ to K **do**
- 6: $\mu_0 := \mathbb{E}[X_0 | x_s]$
- 7: $x_s = x_s - \zeta_t \nabla_{x_s} \|A \mu_0 - y\|$
- 8: $x_s = \mu_s - \sqrt{d} \sigma_t \frac{x_s - \mu_s}{\|x_s - \mu_s\|_2^2}$
- 9: **end for**
- 10: **end for**
- 11: **return** x_0

Algorithm 4 MISR DMAP

Require: $T, K, \{A_i\}_{i=1}^N, \{y_i\}_{i=1}^N, \{\sigma_i\}_{i=1}^N, \zeta_t, d$

- 1: $x_1 = \mathcal{N}(0, I)$
- 2: $w_i := (\sigma_i^2 + \sigma_{\text{floor}})^{-1}$
- 3: $w_i := N \cdot w_i / (\sum_{j=1}^N w_j)$
- 4: **for** $t = 1$ to 0 with T steps **do**
- 5: $x_s \sim p_\theta(X_s | x_t)$
- 6: $\mu_s = \mathbb{E}[X_s | x_t]$
- 7: **for** $j = 1$ to K **do**
- 8: $\mu_0 := \mathbb{E}[X_0 | x_s]$
- 9: $x_s = x_s - \zeta_t \nabla_{x_s} \sum_{i=1}^N [w_i \cdot \|A_i \mu_0 - y_i\|_2^2]$
- 10: $x_s = \mu_s - \sqrt{d} \sigma_t \frac{x_s - \mu_s}{\|x_s - \mu_s\|_2^2}$
- 11: **end for**
- 12: **end for**
- 13: **return** x_0

4. Experiments and Results

Our experiments focus on super-resolution for anisotropic magnetic resonance head images. We consider images that are $4\times$, $8\times$, and $16\times$ worse resolution along through-plane axes than in-plane axes. For HR image volumes of 1 mm^3 isotropic resolution, these *scale factors* correspond to 4, 8, and 16 mm slice thicknesses. To enable quantitative reference-based distortion metrics, we perform simulations of data using Gaussian slice selection profiles with full-width-at-half-max and slice separation equal to the scale factor. Following Eq. 8, we also add Gaussian noise with σ_i proportional to the voxel size due to the physics of how noise interacts with slice selection [44]. Thicker slices have less noise. Specifically, we chose $\sigma_i = 0.1/k_i$, where k_i is the scale factor for the LR image volume y_i .

We used an open-source pre-trained non-latent 3D diffusion model for brain MRI [45]. This model is a flow-estimation model, and we used 64 DDIM steps for all methods and all experiments. This model was trained on more than 70,000 T_1 -weighted brain volumes from 36 open datasets, and additionally withheld two sites from training: AIBL [22] and SLEEP [68]. Thus, to avoid model bias, we selected 50 subjects with 1 mm^3 resolution from each of those two sites as our data cohort. For preprocessing, these image volumes were padded and/or cropped to a voxel size of $192 \times 224 \times 192$ using the center-of-mass location from an HD-BET [30]-calculated brain mask, then linearly normalized to the intensity range $[-1, 1]$ using the volume's minimum and maximum values.

We conducted two experiments. First, we compared SISR to MISR with orthogonal planes. Then, we perform an ablation study and compare noise-weighting to uniform weighting in MISR DPS and MISR DMAP. For evaluation, we used PSNR, SSIM, and when comparing SISR to MISR we additionally calculated the Frechet Inception

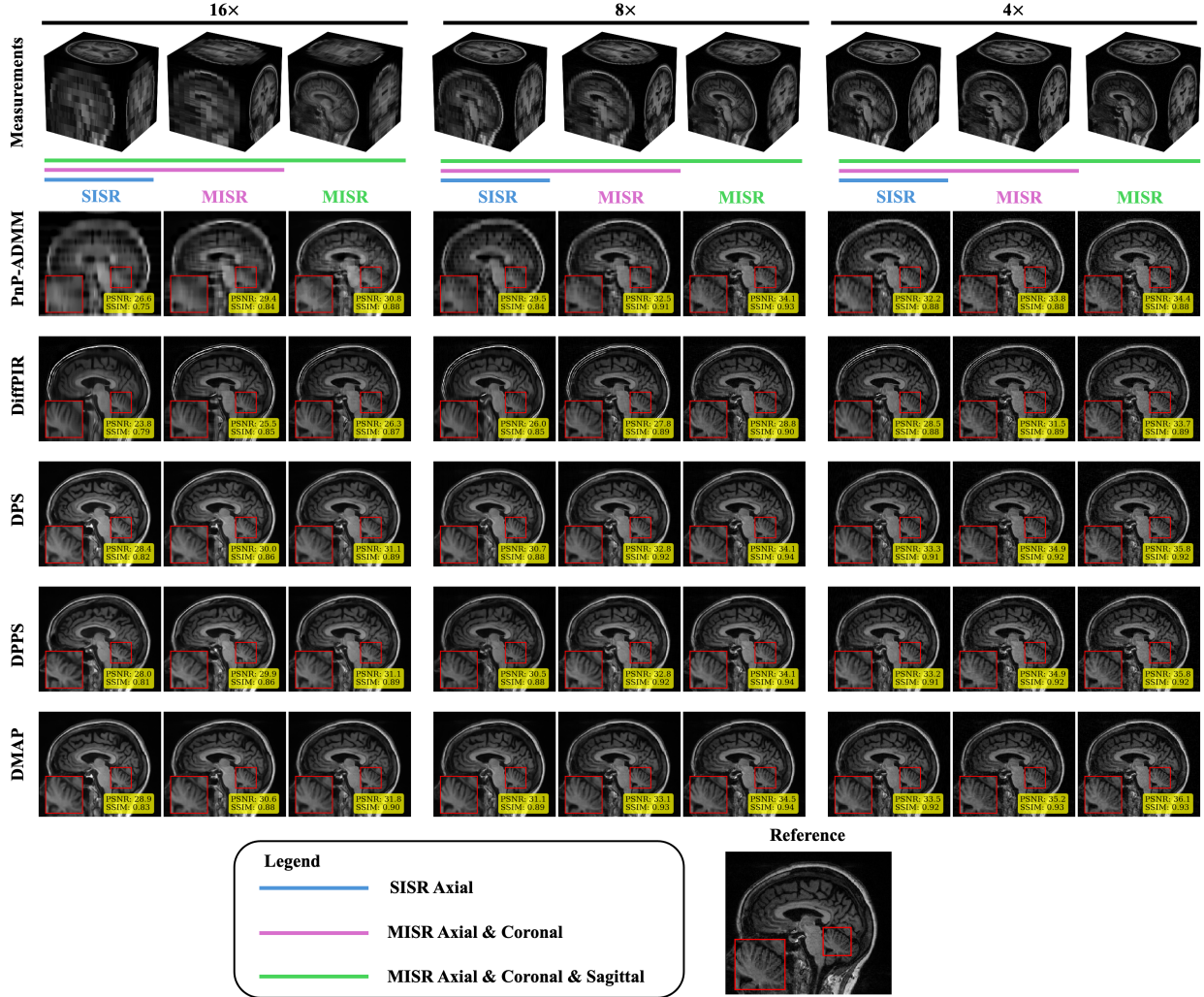


Figure 2. Qualitative results for a representative subject from the AIBL dataset. Row-wise labels designate LR inputs as “Measurements” and SR estimations named by method. Supercolumns group scale factors together. Within supercolumns, each column corresponds to SISR using only the axial acquisition as input (blue), then MISR using axial and coronal (pink), and MISR using axial, coronal, and sagittal (green). The HR reference is shown at the bottom of the figure. For all methods, the same area highlighting the folia of the cerebellum is zoomed into the inset.

Distance (FID) [28, 50]. To enable the computation of FID for 3D volumetric images, we extract 2D slices from each volume from all three cardinal planes, separated by 4 mm, and spanning the center 128 mm of the volume. These slices were linearly normalized to the intensity range [0, 255] using the volume’s minimum and maximum values, quantized to 8-bit integers, and saved to disk as .png files. The reference dataset for the FID computations for the AIBL cohort was the SLEEP cohort, and vice-versa. This was done to prevent an abnormally low FID score due to similar intensity statistics between, for example, true-HR-AIBL and super-resolved-AIBL images.

4.1. SISR vs MISR

In Fig. 1 and Fig. 2, we show qualitative comparisons between slices of representative volumes for SISR and MISR across several methods. We emphasize that all methods operate directly in 3D, and 2D slices are shown for clarity. For MISR scenarios, there are more LR images to use as input, leading to improved results for all methods and scale factors.

In Fig. 3, we show four more representative subjects at 8x scale factor. With a second observation, these regions have more correct anatomy. However, the distortion metrics do not reflect geometric or anatomical errors; the approximately 2 to 3 dB difference in PSNR is not sufficient to describe the improvements gained from another measurement.

Table 1. Quantitative results for 100 subjects. For PSNR and SSIM, the mean \pm std. are reported. FID is computed as mentioned in Sec. 4. Best results by scale factor are **bolded** and second-best results are underlined.

Scale	Method	SISR				MISR			
		Axial		Axial & Coronal		Axial		Axial & Coronal & Sagittal	
		PSNR (\uparrow)	SSIM (\uparrow)	PSNR (\downarrow)	SSIM (\uparrow)	PSNR (\downarrow)	SSIM (\uparrow)	PSNR (\uparrow)	SSIM (\uparrow)
4 \times	PnP-ADMM	31.39 \pm 1.42	0.880 \pm 0.014	98.65	33.30 \pm 1.11	0.883 \pm 0.009	84.97	34.17 \pm 0.91	0.884 \pm 0.008
	DiffPIR	27.92 \pm 1.26	0.888 \pm 0.014	65.44	30.23 \pm 1.19	0.895 \pm 0.009	58.15	32.14 \pm 1.25	0.896 \pm 0.007
	DPS	<u>32.78</u> \pm 2.03	<u>0.918</u> \pm 0.017	41.28	<u>34.59</u> \pm 1.73	<u>0.928</u> \pm 0.012	47.50	35.52 \pm 1.44	<u>0.927</u> \pm 0.009
	DPPS	32.76 \pm 2.04	<u>0.918</u> \pm 0.017	<u>41.19</u>	34.59 \pm 1.74	<u>0.928</u> \pm 0.012	47.30	35.54 \pm 1.42	0.927 \pm 0.009
	DMAP	33.08 \pm 2.14	0.929 \pm 0.018	32.07	34.97 \pm 1.91	0.940 \pm 0.014	34.77	35.98 \pm 1.64	0.940 \pm 0.012
8 \times	PnP-ADMM	28.70 \pm 1.50	0.844 \pm 0.027	158.53	31.51 \pm 1.59	0.914 \pm 0.017	85.09	33.27 \pm 1.67	0.936 \pm 0.013
	DiffPIR	25.18 \pm 1.29	0.857 \pm 0.024	91.66	26.91 \pm 1.25	0.898 \pm 0.016	78.43	27.82 \pm 1.30	0.910 \pm 0.013
	DPS	<u>30.04</u> \pm 2.11	<u>0.878</u> \pm 0.027	39.58	<u>32.21</u> \pm <u>2.07</u>	<u>0.922</u> \pm 0.019	36.25	<u>33.65</u> \pm 2.13	<u>0.940</u> \pm 0.016
	DPPS	30.00 \pm 2.12	0.877 \pm 0.027	<u>39.03</u>	32.18 \pm 2.08	0.922 \pm 0.019	<u>35.84</u>	33.64 \pm 2.15	<u>0.940</u> \pm 0.016
	DMAP	30.36 \pm 2.16	0.888 \pm 0.026	38.97	32.63 \pm 2.13	0.931 \pm 0.019	35.51	34.17 \pm 2.22	0.947 \pm 0.016
16 \times	PnP-ADMM	25.82 \pm 1.33	0.751 \pm 0.037	217.75	28.53 \pm 1.62	0.843 \pm 0.028	126.23	29.98 \pm 1.75	0.881 \pm 0.024
	DiffPIR	23.07 \pm 1.21	0.793 \pm 0.031	116.23	24.68 \pm 1.19	0.856 \pm 0.022	96.28	25.46 \pm 1.20	0.882 \pm 0.019
	DPS	<u>27.56</u> \pm 1.95	<u>0.811</u> \pm <u>0.036</u>	44.61	<u>29.26</u> \pm <u>1.99</u>	<u>0.859</u> \pm <u>0.028</u>	43.93	<u>30.50</u> \pm <u>2.08</u>	<u>0.888</u> \pm <u>0.024</u>
	DPPS	27.47 \pm 1.94	0.810 \pm 0.037	43.98	29.25 \pm 2.01	<u>0.859</u> \pm <u>0.029</u>	42.99	30.47 \pm 2.08	<u>0.888</u> \pm <u>0.024</u>
	DMAP	28.04 \pm 2.03	0.826 \pm 0.036	<u>44.43</u>	29.87 \pm 2.03	0.877 \pm 0.026	43.50	31.25 \pm 2.14	0.905 \pm 0.023

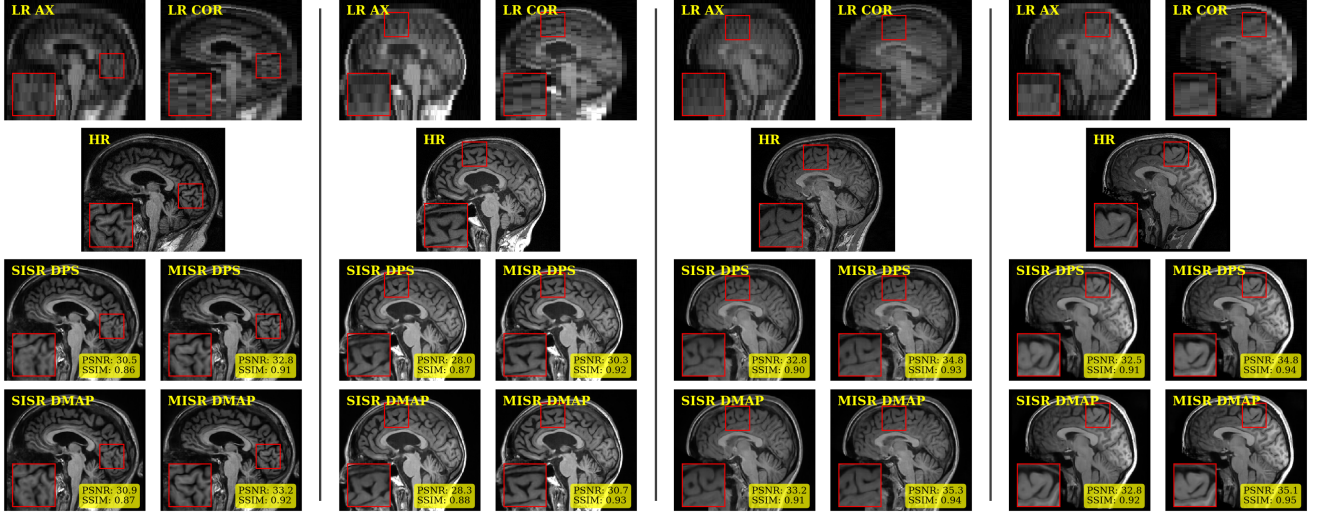


Figure 3. Sagittal slices from four representative subjects are shown for 8× scale factor LR inputs. Each displayed image is labeled for its contents. LR: low-resolution; AX: axial acquisition; COR: coronal acquisition; HR: ground-truth high-resolution; SISR: single-image super-resolution, using the axial acquisition as input; MISR: multi-image super-resolution, using the axial and coronal acquisitions as input. Zoomed inset regions are located by the red box, highlighting anatomical differences that are not correctly recovered by SISR.

We show quantitative results for our 100 subjects in Table 1. In correspondence with the qualitative results from Fig. 2, DMAP outperforms all other methods across the board, both in distortion metrics and FID. An interesting result in Table 1 is the metrics’ trends when adding more LR images. As expected, PSNR and SSIM improve in all cases. However, for the 4× scale factor, the FID score generally worsens for the DPS family of methods as more images are added. This is potentially due to the perception-distortion tradeoff [1]; since the SR image \hat{x} is guided towards being consistent with multiple images, its freedom in being a realistic image is restricted. However, this phenomenon is not present at 8× and 16× scale factors.

4.2. Ablation: noise-weighting

In the previous experiment, each of the LR images used for MISR had the same scale factor. The noise present in the images had the same power, so the noise weights w_i were equal for all i and essentially absorbed into the gradient scalar ζ_t . To evaluate the efficacy of the proposed noise weighting, we compared with and without noise-weighting for mixed-resolution inputs: 4× and 16× scale factors for two orthogonal inputs. We used MISR DPS and MISR DMAP for this evaluation and varied the noise by $\sigma_i = \sigma_{\text{base}}/k_i$, for $\sigma_{\text{base}} = 0.15, 0.3, 0.45$. These values correspond to approximately 1×, 2×, and 3× the average intensity standard deviation in HR images (after normalization to $[-1, 1]$).

In Table 2, we show the results of this experiment. For both MISR DPS and MISR DMAP, noise-weighting improves all metrics. As the noise level becomes more severe, the effect of noise weighting becomes larger.

Table 2. Quantitative results for our ablation without noise weighting (w/o NW) and with noise weighting (w/ NW) for the two-image 4× and 16× scale factors for both MISR DPS and MISR DMAP.

	σ_{base}	w/o NW		w/ NW	
		PSNR (\uparrow)	SSIM (\uparrow)	PSNR (\uparrow)	SSIM (\uparrow)
DPS	0.15	32.5 ± 2.4	0.90 ± 0.01	32.5 ± 2.4	0.90 ± 0.01
	0.3	29.8 ± 1.6	0.78 ± 0.01	29.9 ± 1.6	0.79 ± 0.01
	0.45	27.0 ± 1.1	0.63 ± 0.02	27.5 ± 1.2	0.66 ± 0.02
DMAP	0.15	32.9 ± 2.6	0.91 ± 0.02	32.9 ± 2.6	0.91 ± 0.02
	0.3	30.0 ± 1.6	0.80 ± 0.01	30.1 ± 1.7	0.80 ± 0.01
	0.45	27.2 ± 1.2	0.65 ± 0.01	27.5 ± 1.3	0.67 ± 0.01

5. Conclusion

We presented an approach for MISR using diffusion models. We showed that likelihood separation underneath the diffusion trajectory allows for a flexible multi-image framework and implemented it with noise-weighting for the diffusion posterior sampling family of inverse problem solvers. We conducted experiments at various scale factors with orthogonal acquisition planes and showed that MISR outperforms SISR both qualitatively and quantitatively, and additionally better preserves anatomy. Future work will address misalignment between measurements (though an estimated registration can be folded in to the measurement A) as well as multi-contrast acquisitions. To the best of our knowledge, the results of this work are state-of-the-art in the field of MRI super-resolution for anisotropic image volumes. Our

results indicate that MISR diffusion could make standard 2D MRI acquisitions usable in all viewing planes, potentially reducing the need for long, thin-slice 3D scans and restoring image analytic quality for retrospectively accessed imaging sessions.

References

[1] Yochai Blau and Tomer Michaeli. The perception-distortion tradeoff. In *Proceedings of the IEEE Conference on Computer Vision and Pattern Recognition*, pages 6228–6237, 2018. 8

[2] Ashish Bora, Ajil Jalal, Eric Price, and Alexandros G Dimakis. Compressed sensing using generative models. In *International Conference on Machine Learning*, pages 537–546. PMLR, 2017. 2

[3] Stephen Boyd, Neal Parikh, Eric Chu, Borja Peleato, Jonathan Eckstein, et al. Distributed optimization and statistical learning via the alternating direction method of multipliers. *Foundations and Trends® in Machine learning*, 3(1):1–122, 2011. 5

[4] Robert W. Brown, Y-C Norman Cheng, E. Mark Haacke, Michael R. Thompson, and Ramesh Venkatesan. *Magnetic Resonance Imaging: Physical Principles and Sequence Design (Second edition)*. Wiley, 2014. 3

[5] Antoni Buades, Bartomeu Coll, and Jean-Michel Morel. A review of image denoising algorithms, with a new one. *Multiscale modeling & simulation*, 4(2):490–530, 2005. 2

[6] Emmanuel J. Candès, Justin Romberg, and Terence Tao. Robust uncertainty principles: Exact signal reconstruction from highly incomplete frequency information. *IEEE Transactions on Information Theory*, 52(2):489–509, 2006. 2

[7] Hanqun Cao, Cheng Tan, Zhangyang Gao, Yilun Xu, Guangyong Chen, Pheng-Ann Heng, and Stan Z. Li. A survey on generative diffusion models. *IEEE Transactions on Knowledge and Data Engineering*, 36(7):2814–2830, 2024. 3

[8] Stanley H Chan, Xiran Wang, and Omar A Elgendi. Plug-and-play ADMM for image restoration: Fixed-point convergence and applications. *IEEE Transactions on Computational Imaging*, 3(1):84–98, 2016. 2

[9] Chih-Wei Chang, Junbo Peng, Mojtaba Safari, Elahheh Salari, Shaoyan Pan, Justin Roper, Richard LJ Qiu, Yuan Gao, Hui-Kuo Shu, Hui Mao, et al. High-resolution MRI synthesis using a data-driven framework with denoising diffusion probabilistic modeling. *Physics in Medicine & Biology*, 69(4):045001, 2024. 2

[10] Tianrong Chen, Guan-Horng Liu, and Evangelos Theodorou. Likelihood training of schrödinger bridge using forward-backward SDEs theory. In *International Conference on Learning Representations*, 2022. 3

[11] Ming Cheng, Haoyu Ma, Qiufang Ma, Xiaopeng Sun, Weiqi Li, Zhenyu Zhang, Xuhan Sheng, Shijie Zhao, Junlin Li, and Li Zhang. Hybrid transformer and CNN attention network for stereo image super-resolution. In *Proceedings of the IEEE/CVF Conference on Computer Vision and Pattern Recognition*, pages 1702–1711, 2023. 2

[12] Jooyoung Choi, Sungwon Kim, Yonghyun Jeong, Youngjune Gwon, and Sungroh Yoon. ILVR: Conditioning method for denoising diffusion probabilistic models. In *2021 IEEE/CVF International Conference on Computer Vision (ICCV)*, pages 14347–14356, 2021. 2

[13] Kyobin Choo, Youngjun Jun, Mijin Yun, and Seong Jae Hwang. Slice-consistent 3D volumetric brain CT-to-MRI translation with 2D brownian bridge diffusion model. In *International Conference on Medical Image Computing and Computer-Assisted Intervention*, pages 657–667. Springer, 2024. 3

[14] Hyungjin Chung, Byeongsu Sim, Dohoon Ryu, and Jong Chul Ye. Improving diffusion models for inverse problems using manifold constraints. *Advances in Neural Information Processing Systems*, 35:25683–25696, 2022. 3

[15] Hyungjin Chung, Jeongsol Kim, Michael Thompson Mccann, Marc Louis Klasky, and Jong Chul Ye. Diffusion posterior sampling for general noisy inverse problems. In *The Eleventh International Conference on Learning Representations*, 2023. 2, 3

[16] Hyungjin Chung, Jeongsol Kim, and Jong Chul Ye. Diffusion models for inverse problems. *arXiv preprint arXiv:2508.01975*, 2025. 3

[17] Giannis Daras, Joseph Dean, Ajil Jalal, and Alex Dimakis. Intermediate Layer Optimization for Inverse Problems using Deep Generative Models. In *Proceedings of the 38th International Conference on Machine Learning*, pages 2421–2432. PMLR, 2021. 2

[18] Giannis Daras, Yuval Dagan, Alex Dimakis, and Constantinos Daskalakis. Score-guided intermediate level optimization: Fast Langevin mixing for inverse problems. In *Proceedings of the 39th International Conference on Machine Learning*, pages 4722–4753. PMLR, 2022. 2

[19] Valentin De Bortoli, James Thornton, Jeremy Heng, and Arnaud Doucet. Diffusion Schrödinger Bridge with Applications to Score-Based Generative Modeling. *arXiv preprint arXiv:2106.01357*, 2021. 2

[20] C. Dong, C. C. Loy, K. He, and X. Tang. Image super-resolution using deep convolutional networks. *IEEE Transactions on Pattern Analysis and Machine Intelligence*, 38(2):295–307, 2016. 2

[21] David L Donoho. Compressed sensing. *IEEE Transactions on Information Theory*, 52(4):1289–1306, 2006. 2

[22] Kathryn A. Ellis, Ashley I. Bush, David Darby, Daniela De Fazio, Jonathan Foster, Peter Hudson, Nicola T. Lautenschlager, Nat Lenzo, Ralph N. Martins, Paul Maruff, et al. The Australian Imaging, Biomarkers and Lifestyle (AIBL) study of aging: methodology and baseline characteristics of 1112 individuals recruited for a longitudinal study of Alzheimer’s disease. *International psychogeriatrics*, 21(4):672–687, 2009. 5

[23] Jinsheng Fang, Hanjiang Lin, Xinyu Chen, and Kun Zeng. A hybrid network of CNN and transformer for lightweight image super-resolution. In *Proceedings of the IEEE/CVF conference on computer vision and pattern recognition*, pages 1103–1112, 2022. 2

[24] Chun-Mei Feng, Yunlu Yan, Huazhu Fu, Li Chen, and Yong Xu. Task transformer network for joint MRI reconstruction and super-resolution. In *Medical Image Computing and Computer Assisted Intervention–MICCAI 2021: 24th International Conference, Strasbourg, France, September 27–October 1, 2021, Proceedings, Part VI 24*, pages 307–317. Springer, 2021.

[25] Cristhian Forigua, Maria Escobar, and Pablo Arbelaez. Superformer: Volumetric transformer architectures for mri super-resolution. In *International Workshop on Simulation and Syn*

thesis in Medical Imaging, pages 132–141. Springer, 2022. 2

[26] Ruiqi Gao, Emiel Hoogeboom, Jonathan Heek, Valentin De Bortoli, Kevin P. Murphy, and Tim Salimans. Diffusion Meets Flow Matching: Two Sides of the Same Coin. <https://diffusionflow.github.io/>, 2025. Accessed: 2025-07-09. 2, 3

[27] Zhitao Han and Wenhui Huang. Arbitrary scale super-resolution diffusion model for brain MRI images. *Computers in Biology and Medicine*, 170:108003, 2024. 2

[28] Martin Heusel, Hubert Ramsauer, Thomas Unterthiner, Bernhard Nessler, and Sepp Hochreiter. GANs trained by a two time-scale update rule converge to a local Nash equilibrium. *Advances in Neural Information Processing Systems*, 30, 2017. 6

[29] Jonathan Ho, Ajay Jain, and Pieter Abbeel. Denoising diffusion probabilistic models. *Advances in Neural Information Processing Systems*, 33:6840–6851, 2020. 2, 3

[30] Fabian Isensee, Marianne Schell, Irida Pflueger, Gianluca Brugnara, David Bonekamp, Ulf Neuberger, Antje Wick, Heinz-Peter Schlemmer, Sabine Heiland, Wolfgang Wick, Martin Bendszus, Klaus H. Maier-Hein, and Philipp Kickingereder. Automated brain extraction of multisequence MRI using artificial neural networks. *Human Brain Mapping*, 40 (17):4952–4964, 2019. 5

[31] Kourosh Jafari-Khouzani. MRI upsampling using feature-based nonlocal means approach. *IEEE transactions on medical imaging*, 33(10):1969–1985, 2014. 2

[32] Bahjat Kawar, Gregory Vaksman, and Michael Elad. SNIPS: Solving noisy inverse problems stochastically. *Advances in Neural Information Processing Systems*, 34:21757–21769, 2021. 2

[33] Bahjat Kawar, Michael Elad, Stefano Ermon, and Jiaming Song. Denoising diffusion restoration models. *Advances in Neural Information Processing Systems*, 35:23593–23606, 2022. 2

[34] Eungbean Lee, Somi Jeong, and Kwanghoon Sohn. EBDM: exemplar-guided image translation with brownian-bridge diffusion models. In *European Conference on Computer Vision*, pages 306–323. Springer, 2024. 3

[35] Dawa Chyophel Lepcha, Bhawna Goyal, Ayush Dogra, and Vishal Goyal. Image super-resolution: A comprehensive review, recent trends, challenges and applications. *Information Fusion*, 91:230–260, 2023. 2

[36] Bo Li, Kaitao Xue, Bin Liu, and Yu-Kun Lai. Bbdm: Image-to-image translation with brownian bridge diffusion models. In *Proceedings of the IEEE/CVF Conference on Computer Vision and Pattern Recognition*, pages 1952–1961, 2023. 3

[37] Guangyuan Li, Jun Lv, Yapeng Tian, Qi Dou, Chengyan Wang, Chenliang Xu, and Jing Qin. Transformer-empowered multi-scale contextual matching and aggregation for multi-contrast MRI super-resolution. In *Proceedings of the IEEE/CVF conference on computer vision and pattern recognition*, pages 20636–20645, 2022. 2

[38] Yaron Lipman, Ricky T. Q. Chen, Heli Ben-Hamu, Maximilian Nickel, and Matthew Le. Flow matching for generative modeling. In *The Eleventh International Conference on Learning Representations*, 2023. 3

[39] Xingchao Liu, Chengyue Gong, and Qiang Liu. Flow straight and fast: Learning to generate and transfer data with rectified flow. In *The Eleventh International Conference on Learning Representations*, 2023. 3

[40] Xingchao Liu, Chengyue Gong, et al. Flow Straight and Fast: Learning to Generate and Transfer Data with Rectified Flow. In *The Eleventh International Conference on Learning Representations*, 2023. 2

[41] Zhisheng Lu, Juncheng Li, Hong Liu, Chaoyan Huang, Linlin Zhang, and Tieyong Zeng. Transformer for single image super-resolution. In *Proceedings of the IEEE/CVF conference on computer vision and pattern recognition*, pages 457–466, 2022. 2

[42] José V. Manjón, Pierrick Coupé, Antonio Buades, D. Louis Collins, and Montserrat Robles. MRI superresolution using self-similarity and image priors. *International journal of biomedical imaging*, 2010(1):425891, 2010.

[43] Sachit Menon, Alexandru Damian, Shijia Hu, Nikhil Ravi, and Cynthia Rudin. PULSE: Self-supervised photo upsampling via latent space exploration of generative models. In *Proceedings of the IEEE/CVF Conference on Computer Vision and Pattern Recognition*, pages 2437–2445, 2020. 2

[44] Jerry L. Prince and Jonathan M. Links. *Medical Imaging Signals and Systems*. Pearson, 2015. 5

[45] Samuel W. Remedios, Aaron Carass, Jerry L. Prince, and Blake E. Dewey. Diffusion-Driven Generation of Minimally Preprocessed Brain MRI. *arXiv preprint arXiv:2510.26834*, 2025. 5

[46] Yaniv Romano, Michael Elad, and Peyman Milanfar. The little engine that could: Regularization by denoising (RED). *SIAM Journal on Imaging Sciences*, 10(4):1804–1844, 2017. 2

[47] François Rousseau. Brain hallucination. In *European Conference on Computer Vision (ECCV)*, pages 497–508. Springer, 2008. 2

[48] François Rousseau. A non-local approach for image super-resolution using intermodality priors. *Medical Image Analysis*, 14(4):594 – 605, 2010. 2

[49] Wael Saafin, Miguel Vega, Rafael Molina, and Aggelos K Katsaggelos. Image super-resolution from compressed sensing observations. In *2015 IEEE International Conference on Image Processing (ICIP)*, pages 4268–4272. IEEE, 2015. 2

[50] Maximilian Seitzer. pytorch-fid: FID Score for PyTorch. <https://github.com/mseitzer/pytorch-fid>, 2020. Version 0.3.0. 6

[51] Pradeep Sen and Soheil Darabi. Compressive image super-resolution. In *2009 Conference Record of the Forty-Third Asilomar Conference on Signals, Systems and Computers*, pages 1235–1242. IEEE, 2009. 2

[52] Yuyang Shi, Valentin De Bortoli, Andrew Campbell, and Arnaud Doucet. Diffusion schrödinger bridge matching. *Advances in Neural Information Processing Systems*, 36:62183–62223, 2023. 2, 3

[53] Jiaming Song, Chenlin Meng, and Stefano Ermon. Denoising Diffusion Implicit Models. In *International Conference on Learning Representations*, 2021. 3

[54] Jiaming Song, Chenlin Meng, and Stefano Ermon. Denoising diffusion implicit models. In *International Conference on Learning Representations*, 2021. 3

[55] Jiaming Song, Arash Vahdat, Morteza Mardani, and Jan Kautz. Pseudoinverse-guided diffusion models for inverse problems. In *International Conference on Learning Representations*, 2023. 2

[56] Yang Song, Jascha Sohl-Dickstein, Diederik P Kingma, Abhishek Kumar, Stefano Ermon, and Ben Poole. Score-Based Generative Modeling through Stochastic Differential Equations. In *International Conference on Learning Representations*, 2021. 2

[57] Xuan Su, Jiaming Song, Chenlin Meng, and Stefano Ermon. Dual diffusion implicit bridges for image-to-image translation. In *The Eleventh International Conference on Learning Representations*, 2023. 3

[58] Singanallur V. Venkatakrishnan, Charles A Bouman, and Brendt Wohlberg. Plug-and-play priors for model based reconstruction. In *2013 IEEE Global Conference on Signal and Information Processing*, pages 945–948. IEEE, 2013. 2

[59] Jueqi Wang, Jacob Levman, Walter Hugo Lopez Pinaya, Petru-Daniel Tudosiu, M. Jorge Cardoso, and Razvan Marinescu. InverseSR: 3D brain MRI super-resolution using a latent diffusion model. In *International Conference on Medical Image Computing and Computer-Assisted Intervention*, pages 438–447. Springer, 2023. 2

[60] Yinhuai Wang, Jiwen Yu, and Jian Zhang. Zero-Shot Image Restoration Using Denoising Diffusion Null-Space Model. In *The Eleventh International Conference on Learning Representations*, 2023. 2

[61] Ralph A. Willoughby. Solutions of ill-posed problems. *Siam Review*, 21(2):266, 1979. 2

[62] Jonghye Woo, Ying Bai, Snehashis Roy, Emi Z. Murano, Maureen Stone, and Jerry L. Prince. Super-resolution reconstruction for tongue MR images. In *Proceedings of SPIE—the International Society for Optical Engineering*, page 83140C, 2012.

[63] Zhanxiong Wu, Xuanheng Chen, Sangma Xie, Jian Shen, and Yu Zeng. Super-resolution of brain MRI images based on denoising diffusion probabilistic model. *Biomedical Signal Processing and Control*, 85:104901, 2023.

[64] Zhanxiong Wu, Xuanheng Chen, and Jiangnan Yu. 3D-SRDM: 3D super-resolution of MRI volumes based on diffusion model. *International Journal of Imaging Systems and Technology*, 34(3):e23093, 2024.

[65] Zejun Wu, Samuel W. Remedios, Blake E. Dewey, Aaron Carass, and Jerry L. Prince. AniRes2D: anisotropic residual-enhanced diffusion for 2D MR super-resolution. In *Medical Imaging 2024: Clinical and Biomedical Imaging*, pages 567–574. SPIE, 2024.

[66] Chao Yan, Gen Shi, and Zhengliang Wu. SMIR: A Transformer-Based Model for MRI super-resolution reconstruction. In *2021 IEEE International Conference on Medical Imaging Physics and Engineering (ICMIPE)*, pages 1–6. IEEE, 2021.

[67] Fuzhi Yang, Huan Yang, Jianlong Fu, Hongtao Lu, and Baineng Guo. Learning texture transformer network for image super-resolution. In *Proceedings of the IEEE/CVF conference on computer vision and pattern recognition*, pages 5791–5800, 2020. 2

[68] Michal Rafal Zareba, Magdalena Fafrowicz, Tadeusz Marek, Ewa Beldzik, Halszka Oginska, and Aleksandra Domagalska. Late chronotype is linked to greater cortical thickness in the left fusiform and entorhinal gyri. *Biological Rhythm Research*, 53(10):1626–1638, 2022. 5

[69] Di Zhang, Jiazhong He, Yun Zhao, and Minghui Du. MR image super-resolution reconstruction using sparse representation, nonlocal similarity and sparse derivative prior. *Computers in biology and medicine*, 58:130–145, 2015. 2

[70] Xin Zhang, Edmund Y. Lam, Ed X. Wu, and Kenneth K. Y. Wong. Application of Tikhonov regularization to super-resolution reconstruction of brain MRI images. In *International Conference on Medical Imaging and Informatics*, pages 51–56. Springer, 2007. 2

[71] Zhenting Zhou, Guoping Li, and Guozhong Wang. A hybrid of transformer and cnn for efficient single image super-resolution via multi-level distillation. *Displays*, 76:102352, 2023. 2